Nano Energy 84 (2021) 105950

Contents lists available at ScienceDirect

Nano Energy

journal homepage: http://www.elsevier.com/locate/nanoen

Full paper

MOF encapsulated sub-nm Pd skin/Au nanoparticles as antenna-reactor plasmonic catalyst for light driven CO_2 hydrogenation

Xibo Zhang [a], Yunyan Fan [a], Enming You [a], Zexuan Li [a], Yongdi Dong [a], Luning Chen [a], Ye Yang [a], Zhaoxiong Xie [a,b], Qin Kuang [a,*], Lansun Zheng [a]

[a] State Key Laboratory of Physical Chemistry of Solid Surfaces, Collaborative Innovation Center of Chemistry for Energy Materials, and Department of Chemistry, College of Chemistry and Chemical Engineering, Xiamen University, Xiamen 361005, China
[b] Pen-Tung Sah Institute of Micro-Nano Science and Technology, Xiamen University, Xiamen 361005, China

ARTICLE INFO

Keywords:
Heterogeneous catalysis
Plasmonic catalysis
CO_2 hydrogenation
Metal-organic frameworks (MOFs)
Core shell structure

ABSTRACT

Activation of CO_2 with plasmon induced hot electrons has attracted great attention due to its moderate reaction conditions, but high-efficiency plasmonic catalysts still remains challenging. Herein, we designedly prepared an antenna-reactor plasmonic catalyst with core-shell structure, i.e. sub-nm Pd skin/Au NPs encapsulated within UiO-66-NH_2 (Au@Pd@UiO-66-NH_2-0.5) for CO_2 hydrogenation under light-heat dual activation. Under the photo-thermal synergism, CO_2 can be efficiently converted into CO and the optimal production rate reaches 3737 μmol/g_{metal}/h at 150 °C. Thereinto, ultrafast transient absorption spectroscopy reveals that the sub-nm Pd skin provides a longer time window for hot electron transfer and efficient retardation of energy dissipation. Theoretical calculations further confirm the significant reductions in HOMO-LUMO gap of CO_2 and reaction energy barrier from CO_2* to COOH* through adsorption of CO_2 on sub-nm Pd skin, promoting its efficiency and selectivity. Our findings provide new insights into design of bimetallic plasmonic catalysts for low-temperature catalysis.

1. Introduction

With growing energy needs and environmental concerns, converting greenhouse gas CO_2 into high-value chemicals and fuels is becoming increasingly important technically and economically due to its great potentials in alleviating the current energy and environmental crisis [1–4]. However, traditional thermal activation of CO_2 usually requires relatively high temperatures and pressures owing to its extremely thermodynamic stability and chemical inertness, thereby leading to huge energy consumption coupled with potential safety hazards and high risk of catalyst deactivation [5–7]. To overcome these issues, photo-assisted catalysis has been used as an effective strategy to reduce the energy barrier of chemical reactions [8–17]. Recent advances have highlighted that hot electrons photoexcited in nanostructures of plasmonic metal (such as Au, Ag, Cu and Al) with strong light absorption can be injected into the frontier orbitals of adsorbed species, thereby reducing the activation energies of reactions under much milder conditions than conventional thermocatalysis [12,18–21]. However, the rational design and synthesis of such plasmonic catalysts with high efficiency photo-thermal synergistic catalysis are still challenging.

Bimetallic heterostructures (Au-Pt, Al-Pd, Cu-Ru, etc.) consisting of plasmonic metal (antenna) and reactive metal (reactor) nanostructures, known as "antenna-reactor" plasmonic catalysts, have recently attracted considerable interests due to their fantastic optical properties [22,23] and great potential applications in photocatalysis [12,19,22,24]. In such antenna–reactor architectures, the local field induced by photoexcited plasmonic antenna can drive "forced" plasmons to the adjacent catalysis reactor, thereby directly producing hot electrons in the catalytic reactor to drive chemical processes [25]. The heterometallic "antenna-reactor" plasmonic catalysts mainly have focused on hetero-dimer structure, where the plasmonic metal and active metal are independent components [22,24,26]. Notably, the catalysis efficiency of plasmonic catalysts is highly sensitive to the geometric configuration, such as the shape and size of antenna and reactor, as well as the distance between them [26–28]. Structurally, spherical core-shell heterostructures are more favorable for boosting the plasmonic catalysis efficiency of "antenna-reactor" catalysts than their hetero-dimer counterparts owing to the densely connected and strong interaction between them [29–31]. To

* Corresponding author.
E-mail address: qkuang@xmu.edu.cn (Q. Kuang).

https://doi.org/10.1016/j.nanoen.2021.105950
Received 28 January 2021; Received in revised form 22 February 2021; Accepted 1 March 2021
Available online 3 March 2021

achieve optimal catalysis efficiency, active metal shells serving as reactors should be downsized to the one-nanometer scale for efficient energy transfer from the internal plasmonic antenna to the adsorbed reaction species. However, till now it is still a great challenge to precisely control the architecture of antenna-reactor plasmonic catalysts and clarify key factors behind surface chemical processes.

Herein, novel metal-organic frameworks (MOFs) encapsulated sub-nm (0.5 nm) Pd skin/Au nanoparticles (Au@Pd@UiO-66-NH_2-0.5 NPs) were developed as antenna-reactor plasmonic catalysts for light-driven CO_2 hydrogenation under mild conditions. In this well-designed architecture, the Au NP cores work as an "antenna" to provide an intense localized electric field, while the sub-nm Pd skin play as active sites to activate and hydrogenate CO_2. Our experiments demonstrated that with such sub-nm Pd skin Au NPs being simultaneously encapsulated within amino-modified Zr (IV)-based MOF (UiO-66-NH_2), the highly selective conversion of CO_2 into CO was successfully achieved under illumination. Most strikingly, by controlling the Pd shell at atomic precision, the optimal catalytic activity of such MOF encapsulated sub-nm Pd skin/Au NPs reached 3737 μmol/g_{metal}/h under light-heat dual activation, which is far higher than that of counterparts (Au@UiO-66-NH_2 and Au@Pd@UiO-66-NH_2-2 with 2 nm Pd shell). The influences of the Pd shell thickness and MOF encapsulation structure on the activity and product selectivity of this antenna-reactor plasmonic catalyst were detailedly studied.

2. Experimental section

2.1. Chemicals and materials

Chloroauric acid ($HAuCl_4.4H_2O$, 99.9%), Pd chloride (II) ($PdCl_2$, 99.9%), citrate sodium ($Na_3C_6H_5O_7.2H_2O$, 99%), N, N-dimethylformamide (DMF, 99.5%) and acetic acid (99.5%) were purchased from Sinopharm Chemical Reagent Co., Ltd. Zirconium tetrachloride ($ZrCl_4$, 98%), polyvinyl pyrrolidone (PVP K30), terephthalic acid (H_2BDC, 99%), and 2-aminoterephthalic acid (H_2ATA, 98%) were purchased from Energy Chemical.

2.2. Material synthesis

2.2.1. Synthesis of Au@Pd NPs

First, 100 mL $HAuCl_4.4H_2O$ (0.1 mg/mL) aqueous solution was poured into a 150 mL round bottom flask and heated to 100 °C under constant stirring. Next, 3 mL citrate sodium (10 g/L) was added to the above $HAuCl_4$ aqueous solution to yield a wine-red Au colloidal solution after reaction for about 20 min. The resulting solution was then cooled to room temperature followed by the addition of 0.5 g PVP under stirring for 24 h. The Au colloidal suspension was washed several times with DMF at 17,000 rpm for 20 min and re-dispersed in 20 mL DMF. The as-obtained suspension was heated to 100 °C under stirring followed by the addition of 1 mL H_2PdCl_4 aqueous solution (4 mM/L for Au@Pd-0.5 and 10 mM/L for Au@Pd-2). After 2 h reaction, the color of the suspension changed from wine-red to light purple, and the resulting Au@Pd NPs were filtered off and washed several times with DMF at 13,000 rpm for 10 min

2.2.2. Synthesis of Au@Pd@UiO-66-NH_2-0.5

First, 27.3 mg H_2ATA and 100 mg PVP were dissolved in a mixture of 7 mL DMF and 1.2 mL acetic acid. Next, 1 mL Au@Pd-0.5 NPs dispersed in DMF was added to the mixture and stirred under ultrasounds for 5 min. Meanwhile, an amount of 33.4 mg $ZrCl_4$ was dispersed in 7 mL DMF and then poured into the above mixture and transferred into a 25 mL Teflon-lined stainless-steel autoclave under heating to 120 °C for 24 h. The obtained product was washed several times with DMF and the resulting powder was dried in an oven overnight at 120 °C. Au@UiO-66-NH_2 and Au@Pd@UiO-66-NH_2-2 were obtained under the same conditions by replacing Au@Pd-0.5 with Au NPs and Au@Pd-2 NPs, respectively.

2.2.3. Synthesis of Au@Pd/UiO-66-NH_2-0.5, Au@Pd/P25-0.5 and Au@Pd/SiO_2-0.5

First, 1 mL Au@Pd-0.5 in DMF was dropwise added to 30 mg pre-synthesized UiO-66-NH_2, commercial P25 or commercial SiO_2, and manually ground for 5 min. The resulting Au@Pd/UiO-66-NH_2, *Au@Pd/P25–0.5* and Au@Pd/SiO_2-0.5 was then collected by centrifugation followed by washing several times with DMF and dried overnight in an oven at 120 °C.

2.3. Catalytic tests

2.3.1. Photo-assisted CO_2 hydrogenation measurement of samples

The photo-assisted CO_2 hydrogenation activities of samples were evaluated by vapor-solid reaction mode in a commercial evaluation system (CEL-HPR100T+, Beijing China Education Au-Light Co., Ltd, Fig. S5). To this end, 5 mg catalyst was evenly dispersed on a quartz chip and transferred into a 150 mL stainless steel reactor with a quartz window (diameter: 3.5 cm) and compensatory heating side. After sealing, the reactor was flushed several times to remove the air and then filled with 1 MPa CO_2/H_2 mixed gas (CO_2:H_2 =1:3). Next, the reactor was irradiated by a 300 W Xe lamp (CEL-HXF300, Beijing China Education Au-Light Co., Ltd.). Meanwhile, the reactor temperature (typically 150 °C) was controlled by a thermocouple and heating system connected to the reactor under both dark and light experiments. The final products were detected by gas chromatography (SHIMADXU GC-2014C) equipped with a flame ionization detector and thermal conductivity detector. UV cut-off filter ($\lambda < 400$ nm) and ($400 < \lambda < 650$ nm) filters were used to explore the influence of light wavelength on the efficiency of catalysts toward the CO_2 hydrogenation.

2.4. Numerical calculation of scattering and heat generation

All the numerical calculations were performed by COMSOL Multiphysics based on finite element methods. The calculation was divided into two steps, where the electromagnetic scattering of the nanostructure was solved first and then the heat generation of the system was calculated. In the first step, a scattered-field formulation was used, where the background field was solved analytically through Fresnel's law in absence of the nanoparticles. The incident power was 900 mW/cm^2, which was the same as experiments. The diameters of MOF and gold core were 150 nm and 14 nm, and the thickness of palladium shell was 0.5 nm or 2 nm. The permittivity of gold and palladium were taken from experimental data measured by Johnson and Chrwasty [32,33]. In the second step, the heat generation was calculated based on the steady-state heat transfer model. The heat power volume density Q_d, which was contributed by the heat generated in the materials, was written as

$$Q_d = \frac{1}{2}\varepsilon_0 \omega \mathrm{Im}(\varepsilon_r)|\boldsymbol{E}|^2$$

where ε_0 was the permittivity of vacuum; ω was the angular frequency of the light; ε_r was the relative permittivity of the material; E was electric field. The thermal diffusion equation in the steady-state regime was written as

$$\nabla \cdot (-k\nabla T) = Q_s$$

where k was the thermal conductivity; T was the temperature; Q_s was the power density of heat source. The thermal conductivity of UiO-66-NH_2 air, gold and palladium were 0.11 W/(m·k), 0.03 W/(m·k), 317 W/(m·k) and 71.8 W/(m·k) respectively.

2.5. Measurement of transient absorption spectroscopy

The ultrafast laser used in our experiment was generated by the Ti: sapphire ultrafast laser amplifier (Coherent Astrella, 800 nm, pulse duration ~35 fs, ~7 mJ/pulse and 1 KHz repetition rate) and was split into two beams by a beam splitter. One part was sent into an optical parametric amplifier (OPerA Solo, Coherent) to generate pump light whose center wavelength was 500 nm; meanwhile, the other part was focused on the sapphire crystal to obtain white light continuum (430–820 nm) as probe light to examine the absorption change of samples. The delay between pump light and probe light was tuned by the delay line (minimum step: 50 fs; maximum delay: ~5 ns). The sample was dispersed into ultrapure water to obtain the homogeneous colloidal solution and put into a quartz colorimetric dish with 1 mm thickness. The pump and probe light were focused and overlapped onto the sample colloidal solution. The power of the pump light was controlled by a neutral density filter wheel to 114 μW and the pump beam size was ~1.6 mm. All the measurements were under ambient condition.

2.6. Theoretical calculation

Spin-polarized first-principles calculations were performed based on density functional theory. The generalized gradient approximation (GGA) of Perdew-Burke-Ernzerhof (PBE) function was selected for the exchange-correlation potentials [34]. The double numeric plus polarization (DNP) basis set was used in the local atomic orbital basis set with the global orbital cutoff 4.5 Å. The convergence criterion for the self-consistent field (SCF) was set to 1.0 e^{-6} au. The model structure was optimized until the maximum force was below 0.001 Ha/Å. The equilibrium lattice constants were optimized with maximum stress on each atom within 0.05 eV/Å. The Hubbard U (DFT+U) corrections for metals were set according to the literature [35].

The free energy was calculated using the equation:

$$G = E + ZPE - TS$$

where *G, E, ZPE* and *TS* are the free energy, total energy from DFT calculation, zero-point energy, and entropic contributions (*T* was set to be 300 K), respectively.

3. Results and discussion

The synthetic route of the proposed Au@Pd@UiO-66-NH_2 plasmonic catalysts is provided in Fig. 1a. First, PVP capped Au NPs (average size of

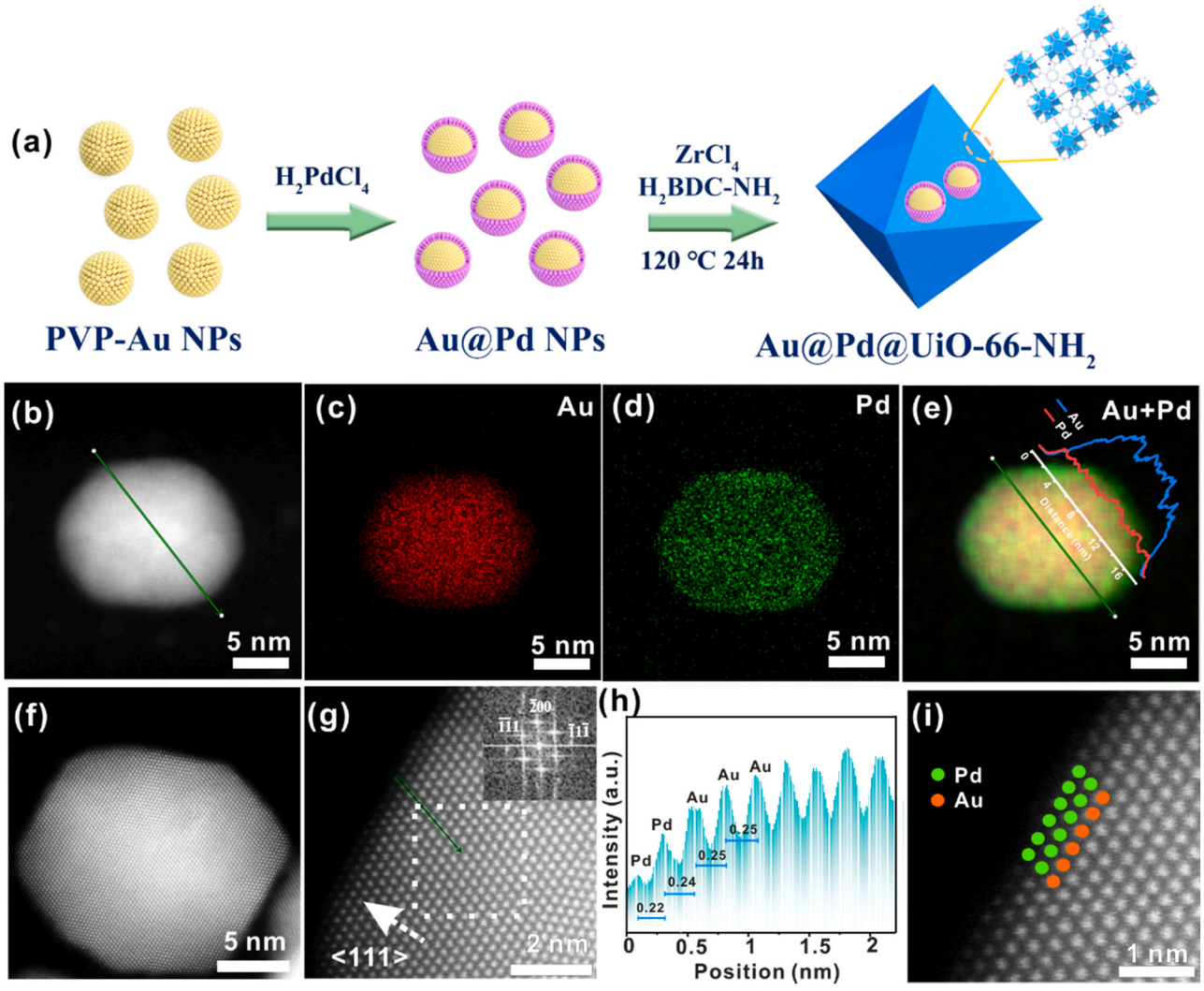

Fig. 1. (a) Schematic illustration of the synthesis process of Au@Pd@UiO-66-NH_2. (b) Cs-corrected HADDF-STEM image of individual Au@Pd-0.5 NP and (c, d and e) corresponding EDS elemental maps. (insert EDS elemental line profiles taken along the green line in e). (f) Low magnification atomic-resolution image. (g) High magnification atomic-resolution image taken from the edge region of Au@Pd-0.5 NP. The inset corresponds to an FFT image of the selected region in (g). (h) The atomic distances along the green line in (g). (i) Magnified atomic-resolution image and corresponding atomic arrangement.

13.8 nm) were synthesized by the conventional sodium citrate reduction method [36]. A seed-mediated growth was then conducted to form Au@Pd NPs with core-shell structures. In this process, the thickness of Pd shell deposited on Au seed could precisely be controlled from sub-nm (0.5 nm) to 2 nm by adjusting the amount of Pd precursor (H_2PdCl_4). Next, the resulting Au@Pd NPs were encapsulated within UiO-66-NH_2 with strong adsorption ability toward CO_2 to protect Au@Pd NPs from aggregation. To observe the structure evolution of products, transmission electron microscopy (TEM) characterization was detailedly conducted on the Au@Pd NPs with 0.5 nm Pd shell before and after encapsulation (i.e., Au@Pd-0.5 and Au@Pd@UiO-66-NH_2-0.5). Compared to the initial Au seeds, the diameter of Au@Pd-0.5 NPs increases to 14.6 ± 1.3 nm (Fig. S1). The spherical aberration (Cs) corrected high-angle annular dark-field scanning transmission electron microscopy (HAADF-STEM) image and corresponding elemental mappings show the surface of Au NPs is covered by a thin layer of Pd (Fig. 1b–e). To determine the accurate thickness of Pd shell, atomic-resolution Cs-corrected HADDF-STEM images were recorded and the results are displayed in Fig. 1f–g. The whole Au@Pd-0.5 particle exhibits continuous atom arrangements corresponding to (111) planes. However, a careful survey reveals slightly smaller interatomic distances of the two most superficial atomic layers of NP when compared to the

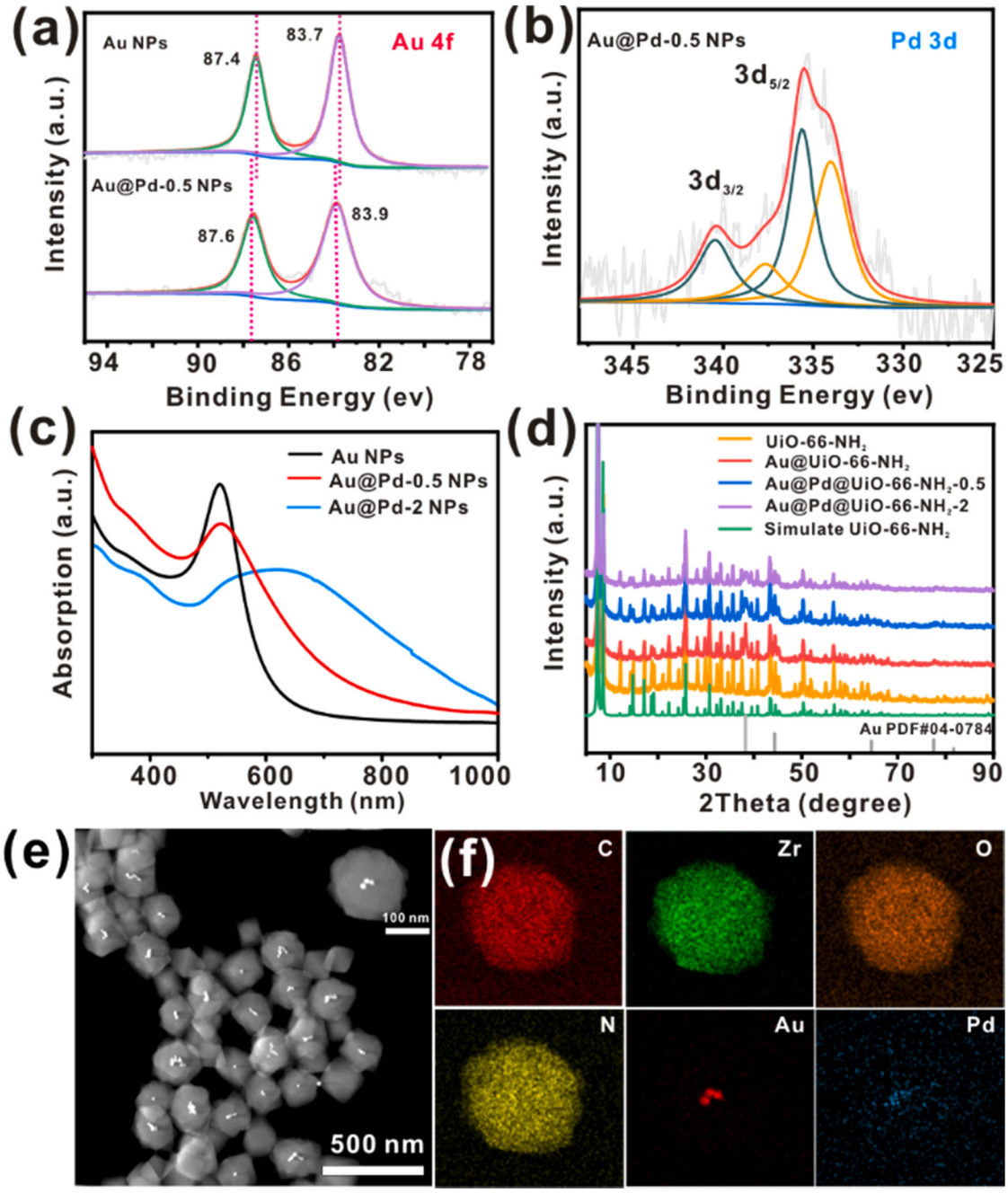

Fig. 2. (a) Au 4f high-resolution XPS spectra of Au NPs and Au@Pd-0.5 NPs. (b) Pd 3d high-resolution XPS spectra of Au@Pd-0.5 NPs. (c) UV–vis spectra of Au NPs, Au@Pd-0.5 NPs, and Au@Pd-2 NPs. (d) Powder XRD patterns of UiO-66-NH_2, Au@UiO-66-NH_2, Au@Pd@UiO-66-NH_2-0.5, Au@Pd@UiO-66-NH_2-2, and simulate UiO-66-NH_2. (e) HAADF-STEM image of Au@Pd@UiO-66-NH_2-0.5 catalysts. The inset shows a magnified image of single Au@Pd@UiO-66-NH_2-0.5. (f) Corresponding EDS maps of single Au@Pd@UiO-66-NH_2-0.5 in (e).

inner region, which should be caused by the smaller atomic diameter of Pd with respect to that of Au (Fig. 1h–i). These results reveal that the shell is only composed of two layers of Pd atoms with a thickness of ca. 0.5 nm, consistent with the increase in the Au@Pd-0.5 NPs size.

The structural homogeneity of such sub-nm Pd skin/Au NPs was further confirmed by cyclic voltammetry measurements. In the first cycle, only a well-defined Pd oxide reduction peak emerges at 0.78 V (Fig. S2), indicating Au NPs are fully covered by ultrathin Pd shells. The Pd shell lattices slightly expand due to the effect of Au core, which influences the electronic structures of Au@Pd NPs [37]. X-ray photoelectron spectroscopy (XPS) analyses showed that Au 4f peaks of Au@Pd-0.5 NPs shift to higher binding energies when compared to pristine Au NPs, suggesting electron transfer from Au to Pd (Fig. 2a and b). Additionally, after the coverage of Au NPs by Pd atoms, the LSPR absorption peak of Au at 520 nm becomes significantly broad (Fig. 2c) [38,39]. All these results indicate that the electronic structure of Au@Pd-0.5 NPs is different from that of Au NPs due to the introduction of such sub-nm Pd shell.

The resulting sub-nm Pd skin/Au NPs were then encapsulated in UiO-66-NH_2 by a simple solvothermal route using 2-aminoterephthalic acid (H_2ATA, 98%) and $ZrCl_4$ as sources and DMF as solvent at 120 °C for 24 h. Powder X-ray diffraction (PXRD) reveals tha all the diffraction peaks of Au@Pd@UiO-66-NH_2-0.5 match well with the simulated pattern of UiO-66-NH_2 except for the weak peak at 38° related to Au (111) plane (Fig. 2d). Meanwhile, the diffraction peaks of Pd are absent due to its relatively lower content (0.17 wt%) compared to Au (1.20 wt %) in Au@Pd@UiO-66-NH_2-0.5. And the contents of Au and Pd in Au@Pd@UiO-66-NH_2-2 is 1.32 wt% and 0.36 wt% obtained by ICP- MS. The SEM images of UiO-66-NH_2 are shown in Fig. S3. After the encapsulation of Au@Pd-0.5 NPs in UiO-66-NH_2, the whole particles display irregular polyhedral shapes with diameters of 150–200 nm (Fig. S4). The HAADF-STEM images and corresponding element mapping images (Fig. 2e and f) reveal more than one Au@Pd NPs are encapsulated in the central region in most Au@Pd@UiO-66-NH_2-0.5 particles. Such status of one-to-many encapsulation of Au@Pd NPs within UiO-66-NH_2 will enhance the catalytic performance of plasmonic catalysts since the plasmonic coupling induced by interparticle interactions can further intensify the electromagnetic energy in the nearfield centered on the nanostructures [40].

The catalytic properties of as-obtained Au@Pd@UiO-66-NH_2-0.5 toward CO_2 hydrogenation were evaluated in the gas-solid phase of a 150 mL batch reactor. (Fig. S5). Two control catalysts (Au@UiO-66-NH_2 and Au@Pd@UiO-66-NH_2-2) were prepared to investigate the role of Pd shell, which were respectively encapsulated with the pristine Au NPs (Fig. S6) and Au@Pd NPs with 2 nm shell (Fig. S7). Compared to Au@UiO-66-NH_2, the Au LSPR peak of Au@Pd@UiO-66-NH_2 at 520 nm significantly weakens or vanishes as the thickness of Pd shell increases (Fig. S8) [41]. Furthermore, the Zr 3d high-resolution XPS spectra of Au@Pd@UiO-66-NH_2-0.5 and Au@UiO-66-NH_2 significantly shift to lower binding energies when compared to UiO-66-NH_2, indicating strong interactions between metals and UiO-66-NH_2 (Fig. S9) [42].

The catalytic activities of Au@Pd@UiO-66-NH_2-0.5 toward the CO_2 hydrogenation reaction are gathered in Fig. 3a. Without illumination, the CO_2 molecules cannot be activated at room temperature, and no products are detected even at an elevated temperature of 150 °C. By contrast, CO_2 is efficiently transformed into CO over Au@Pd@UiO-66-NH_2-0.5 under irradiation of 300 W Xe lamp without additional heating, with the CO production rate reaching 758 μmol/g_{metal}/h. As the reaction temperature rises, the CO production rate significantly increases and reaches a maximum of 3737 μmol/g_{metal}/h at 150 °C, which is 5-fold higher than that obtained solely by light without heat (Fig. 3b). Additionally, the photocatalytic rate using Au@Pd@UiO-66-NH_2-0.5 catalyst varies linearly with the light intensity (Fig. S10), indicating that the catalytic reaction over Au@Pd@UiO-66-NH_2-0.5 follows the hot electrons driven mechanism [9,10]. Also, the CO production rate over Au@Pd@UiO-66-NH_2-0.5 varies linearly with the reaction time (Fig. S11). The TEM and XRD analyses of recycled catalysts demonstrate that the morphology and structure of Au@Pd@UiO-66-NH_2-0.5 is well

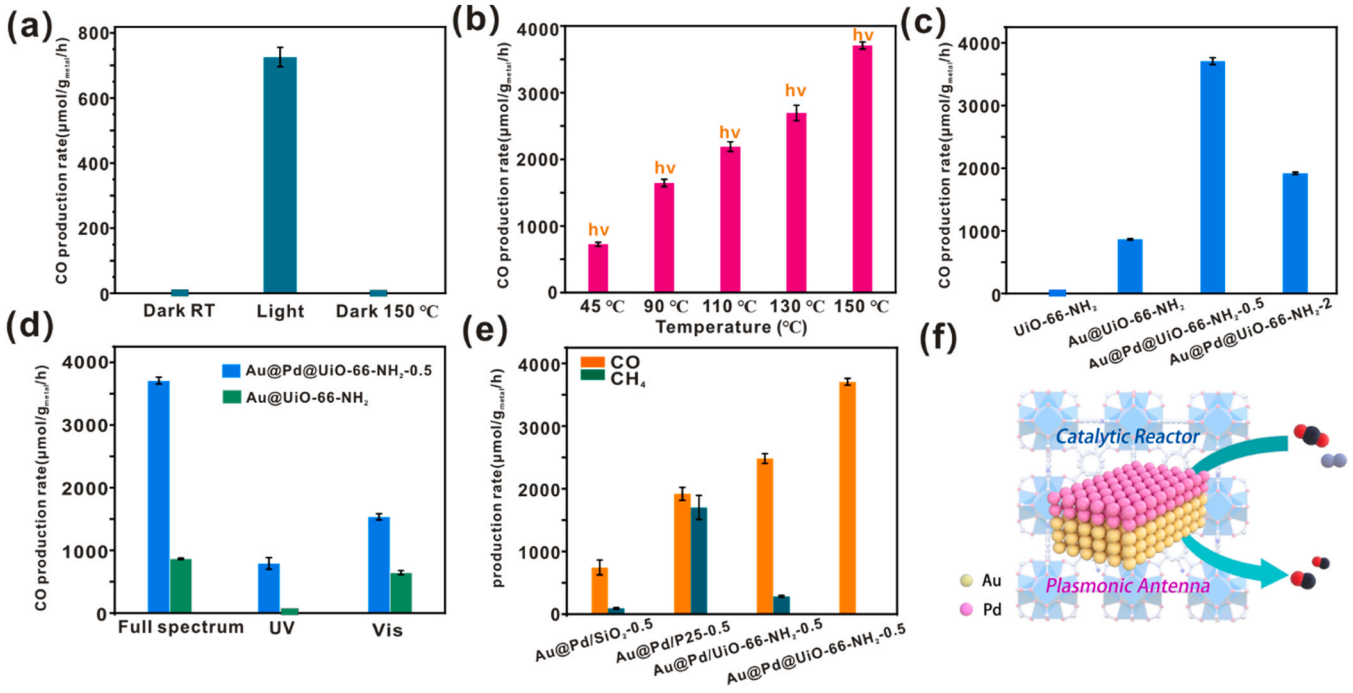

Fig. 3. (a) CO production rates using Au@Pd@UiO-66-NH_2-0.5 under dark at room temperature, under irradiation with a 300 W Xe lamp, and under dark at 150 °C. (b) CO production rates using Au@Pd@UiO-66-NH_2-0.5 at different temperatures under illumination. Production rates obtained by the prepared catalysts consisting of different: (c) metallic catalysts, (d) wavelengths, and (e) loading styles at 150 °C under illumination. (f) Scheme of the core-shell structure of Au@Pd@UiO-66-NH_2-0.5.

maintained after reaction under illumination at 150 °C for 6 h (Fig. S12). It is worth noting that the CO production rate per unit time started to decline slightly when reaction time was further extended to 8 h. To confirm the performance stability of Au@Pd@UiO-66-NH_2-0.5, cycling test were conducted. The cycling test shows that the catalytic performance dropped by 24% at second cycle and maintained by 62% at third cycle (Fig. S13). TEM images of the sample after the cycling testing suggested that nanoparticles underwent sintering and the part of the MOF structure is broken (Fig. S14).

The catalytic activities of CO_2 hydrogenation of Au@UiO-66-NH_2, Au@Pd@UiO-66-NH_2-2, and the blank UiO-66-NH_2 were measured under the same conditions. As shown in Fig. 3c, no product is detected over UiO-66-NH_2. By comparison, a CO production rate of 876 μmol/g_{metal}/h is achieved over Au@UiO-66-NH_2, less than 1/4 of that recorded over Au@Pd@UiO-66-NH_2-0.5. However, the catalytic activity of Au@Pd@UiO-66-NH_2 catalyst (Au@Pd@UiO-66-NH_2-2) decreases sharply to half (1911 μmol/g_{metal}/h) of that of Au@Pd@UiO-66-NH_2-0.5 when the thickness of the Pd shell increases to 2 nm. Undoubtedly, Pd serving as a 'reactor' material is more active toward CO_2 hydrogenation than Au, and the enhancement effect of Pd shell strongly depends on its thickness. Besides, the sub-nm Pd shell exhibits distinct enhancement effects under different wavelengths when compared to Au cores (Fig. 3d). In particular, the activity of Au@Pd@UiO-66-NH_2-0.5 in the visible light region ($400 < \lambda < 650$ nm) is twice that obtained in the ultraviolet region ($\lambda < 400$ nm). It is possible that there is more energy transfer to the Pd shell in this wavelength range ($400 < \lambda < 650$ nm) due to the difference in dielectric function of Au to Pd [31].

To explore the role of the MOF encapsulated structure, different carriers and loading status of Au@Pd NPs are further tested (Figs. S15 and S16). For Au@Pd-0.5 NPs supported on inert SiO_2 carrier, CO_2 can be converted into CO accompanied by small amounts of CH_4 and the CO production rate is only 788 μmol/g_{metal}/h (Fig. 3e and Table S1). When Au@Pd-0.5 NPs supported on TiO_2, CO_2 is converted into CO and CH_4, with the production rate reaching 1920 μmol/g_{metal}/h and 1702 μmol/g_{metal}/h. (Fig. 3e and Table S1). The poor CO selectivity may be related to the form of CO_2 adsorbed on TiO_2. By comparison, Au@Pd/UiO-66-NH_2-0.5 built with Au@Pd-0.5 NPs directly loaded on MOF shows enhanced catalytic activity reaching 2494 μmol/g_{metal}l/h. However, the activity of Au@Pd/UiO-66-NH_2-0.5 greatly reduces and small amounts of CH_4 are produced in addition to CO when compared to Au@Pd@UiO-66-NH_2-0.5 with an encapsulated structure. Thus, the encapsulation process enables UiO-66-NH_2 shell with better CO_2 enrichment effect and stronger interaction with active metal catalysts, greatly improving the catalytic activity [43,44]. Additionally, the MOF shell have the ability to control the adsorption states of reactant/product molecules on the catalyst surface, thereby improving the product selectivity [45–49]. To the best of our knowledge, the Au@Pd@UiO-66-NH_2-0.5 also exhibited an excellent activity performance compared with other representative catalysts recently reported (Table S2). A schematic diagram of light-driven CO_2 hydrogenation over Au@Pd@UiO-66-NH_2-0.5 is displayed in Fig. 3f.

The above data reveal the importance of both the thickness of Pd shell and MOF encapsulation structure in controlling the activity and product selectivity of such special antenna-reactor plasmonic catalysts. Hence, theoretical simulation and ultrafast transient absorption (TA) spectroscopy were conducted to clarify the enhancement mechanism. As we know, plasmonic metallic nanostructures have the ability to convert light to thermal energy via electron–phonon coupling, thus providing localized heating (i.e., the photothermal effect), which is considered to be another possible reason for improving the performances of plasmonic hybrid photocatalysts [50]. In general, only strong light intensity will create an obvious photothermal effect [10]. To this end, The steady temperatures of Au and Au@Pd NPs encapsulated within UiO-66-NH_2 at 520 nm illumination were first simulated by COMSOL Multiphysics based on finite element methods to confirm the photothermal effect on the catalytic performances [51]. The increased steady-state

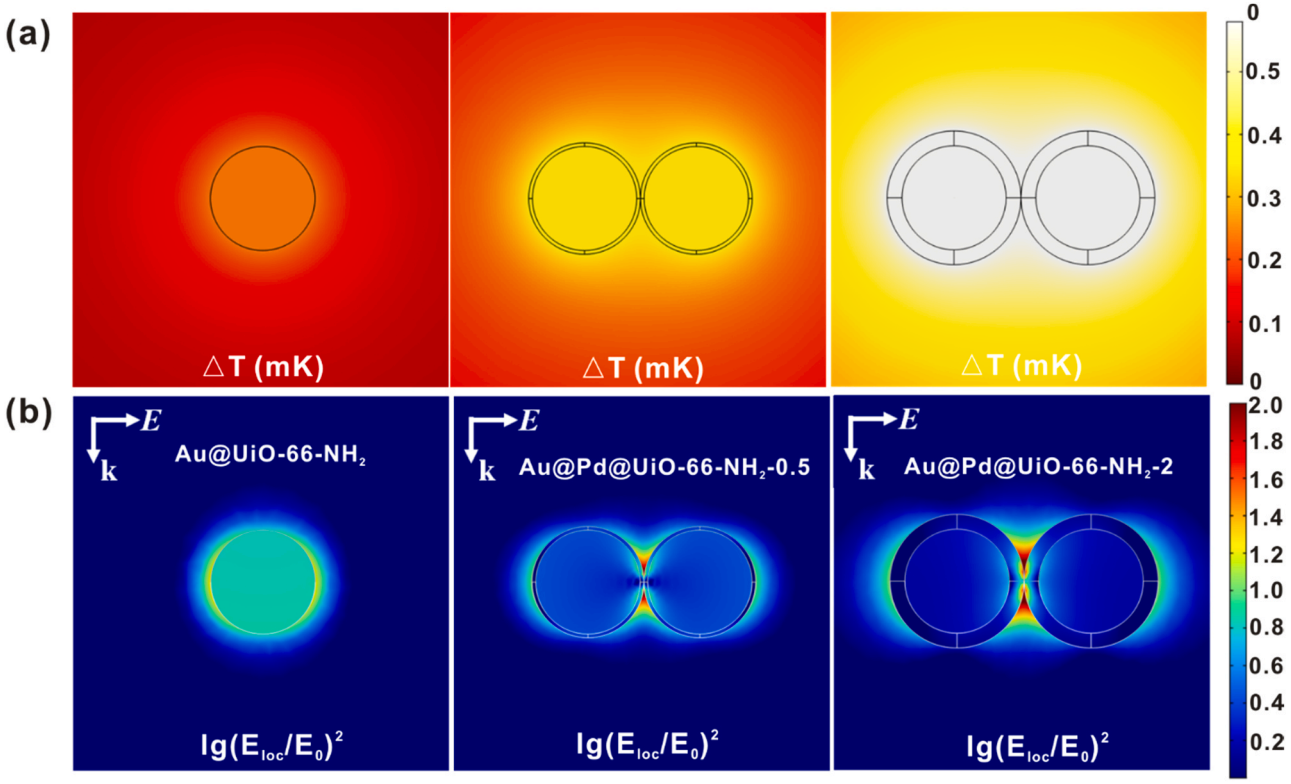

Fig. 4. (a) Increase in steady-state temperature caused by 520 nm light excitation at an incident power density of 0.9 W/cm^2. (b) Enhanced electric field distributions of Au@UiO-66-NH_2, Au@Pd@UiO-66-NH_2-0.5, and Au@Pd@UiO-66-NH_2-2. E_{loc} represents the local electric field and E_0 is the incident electric field.

temperatures of Au@UiO-66-NH_2, Au@Pd@UiO-66-NH_2-0.5 and Au@Pd@UiO-66-NH_2-2 are recorded as 0.24, 0.36 and 0.58 mK, respectively (Fig. 4a). Thus, the results indicated that there were differences in relative heating between two types of nanoparticles. On the other hand, the electric field enhancement distributions of related samples were also simulated. As shown in Fig. 4b, the Au core acts as an "antenna" to generate strong localized electromagnetic fields, as well as enhances the near field of the Pd shell. For Au@Pd@UiO-66-NH_2, multiple Au@Pd NPs are encapsulated together within UiO-66-NH_2 to generate hot spots between them and accelerate the production of hot electrons [40]. However, the light absorption of the Au@Pd NPs with thick Pd shell significantly weakens (Figs. S8 and S17). This result partly accounts for the lower activity of Au@Pd@UiO-66-NH_2-2 compared to Au@Pd@UiO-66-NH_2-0.5.

To further explore the plasmon-enhanced reaction mechanism, ultrafast TA measurements were carried out to track the carrier dynamics in plasmonic Au, Au@Pd-0.5, and Au@Pd-2. In Fig. 5a, the negative bleach signals around 520 nm with the two positive wings have been attributed to the broadening of plasmon band [52]. The decay of these features reflects the carrier and lattice cooling. The hot carriers quickly dissipate their excess energy to the lattices via electron-phonon (e-p) coupling, which is followed by a slower heat transfer from the lattice to environment via phonon-phonon scattering (p-p). Thus, the kinetics of the plasmon band bleach can be described by a two-step cooling model [52,53]. As shown in Fig. 5b, the kinetics fitting reveals that the e-p processes in Au@Pd-0.5 (τ_1 = 0.7 ps) and Au@Pd-2 (τ_1 =0.6 ps) are faster than that in Au (τ_1 =1.6 ps). This phenomenon is likely due to the larger electron-phonon coupling constant in Pd (8.7×10^{17} W m^{-3} K^{-1}) when compared to that of Au (3.0×10^{16} W m^{-3} K^{-1}) [54]. In contrast to Au@Pd-2, Au@Pd-0.5 with sub-nm Pd shell exhibits a longer hot-electron decay time. As a result, the presence of sub-nm Pd skin could provide a longer time window for additional hot electron transfer process. Meanwhile, the p-p rate also declines as thickness of Pd increases, suggesting efficient retardation of energy dissipation caused by the Pd shell [54,55]. In other words, the Pd shell helps to retain the energy gained from photon absorption within the NPs for a longer duration. Therefore, it is necessary to precisely control the thickness of Pd shell on plasmonic Au core in order to obtain the optimal catalytic activity.

In general, the electronic structure of CO_2 molecules would change after adsorption on metal surfaces [10,56,57]. To explore the influence of Pd shell on the surface chemical reactions, the electronic structures were calculated for free CO_2 adsorbed on Au sites in Au@UiO-66-NH_2, as well as free CO_2 adsorbed on Pd and Zr sites at the interface of Au@Pd-0.5 and UiO-66-NH_2 in Au@Pd@UiO-66-NH_2-0.5. As shown in Fig. 6a, the LUMO (2π antibonding) of CO_2 decreases significantly after the adsorption of CO_2 on the metal surface. The gap between HOMO (5σ bonding) and LUMO (2π*) reduces from 8.5 eV for free CO_2 molecules to 3.1 eV for CO_2 adsorbed on Pd surface. This change is much lower than those of CO_2 adsorbed on Au (4.6 eV) and Zr sites at the interface between Au@Pd-0.5 and MOF (3.5 eV). The reason for this has to do with the adsorption of CO_2 on Pd shell, which facilitates the jump of hot-electrons into LUMO of CO_2 under light irradiation due to the significantly reduced gap [10].

First-principles calculations based on spin-polarized density functional theory (DFT) and generalized gradient approximation (GGA) were further used to study the adsorption of CO_2 molecules at different sites of the catalysts. The differential charge densities of CO_2 at Au sites of Au@UiO-66-NH_2, Pd, and Zr sites in Au@Pd@UiO-66-NH_2-0.5 are shown in Fig. 6b. The charge transfer values between CO_2 and each site are estimated to 0.17 eV at Au, 0.31 eV at Pd, and 0.23 eV at Zr. The electron transfer between CO_2 and Pd sites looks more obvious than others. Besides, the free energies of different reaction paths over Au@UiO-66-NH_2 and Au@Pd@UiO-66-NH_2-0.5 are calculated to rationalize the activity and selectivity of catalysts for photothermal CO hydrogenation (Figs. S18–S21). The rate-determining step of the reaction is determined as the formation of COOH* from CO_2* [58]. As shown in Fig. 6c, the sub-nm Pd shell effectively reduces the energy barrier for the generation of COOH* from 1.867 eV to 0.878 eV. According to the free energies of producing CO and CH_4, the reaction is more inclined to

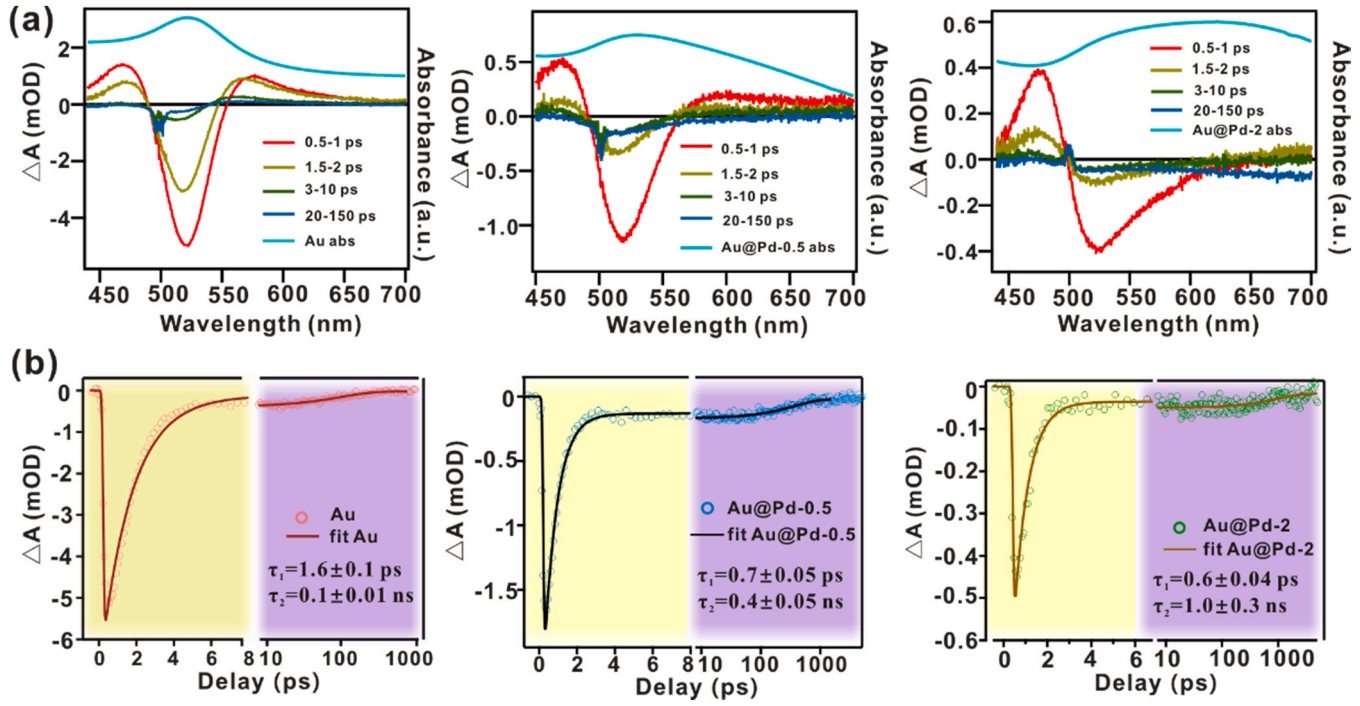

Fig. 5. (a) Ultrafast TA spectroscopy of Au, Au@Pd-0.5, and Au@Pd-2. (b) TA signals from kinetic curves of Au, Au@Pd-0.5, and Au@Pd-2 (τ_1: electron-phonon scattering and τ_2: phonon-phonon scattering).

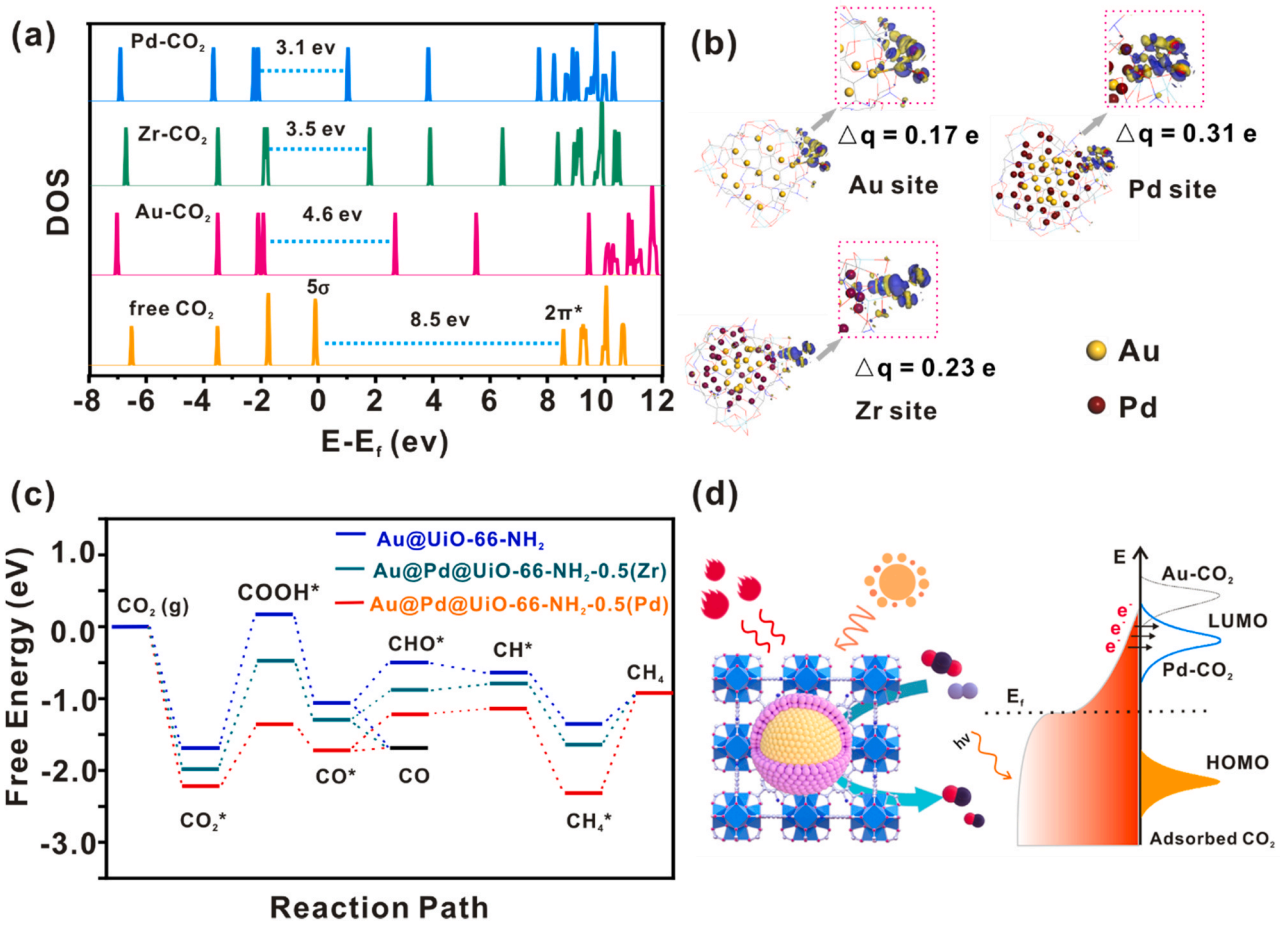

Fig. 6. (a) The electronic structures of free CO_2, as well as CO_2 adsorbed on Au sites in Au@UiO-66-NH_2, Pd, and Zr sites in Au@Pd@UiO-66-NH_2-0.5. (b) Differential charge densities of CO_2 at different sites. The isosurface value is 0.03 eV/Å^3. (c) Free energies of different reaction paths over different catalysts and active sites. (d) Schematics of light driven CO_2 hydrogenation over Au@Pd@UiO-66-NH_2-0.5.

produce CO, which is in line with our experimental results. It is worth noting that a comparison between the free energies of the two different reaction paths suggests that CO_2 is more favorable to activate on the Pd surface [59]. In short, the adsorption of CO_2 on sub-nm Pd skin significantly reduces the HOMO-LUMO gap of CO_2, as well as the reaction energy barrier from CO_2* to COOH*. This, in turn, promotes the hot electrons for injection into the LUMO orbitals of CO_2, leading to efficient surface reactions (Fig. 6d).

4. Summary

A novel plasmonic catalyst made of sub-nm Pd skin/Au NPs encapsulated within UiO-66-NH_2 was successfully prepared for the CO_2 hydrogenation reaction under light-heat dual activation. The hot electrons excite by light effectively activated the CO_2 molecules under Xe lamp irradiation and the CO production rate reaches 3737 μmol/g_{metal}/h at 150 °C. The ultrathin Pd shell of 0.5 nm in Au@Pd@UiO-66-NH_2-0.5 significantly improves the catalytic activity. Besides, the encapsulation structure of UiO-66-NH_2 promotes the conversion and selectivity to CO due to the elevated adsorption capability towards CO_2 and strong confinement effect of MOFs. The ultrafast TA spectroscopy data revealed that the thickness of Pd shell greatly affected the decay process of the plasmon. The theoretical calculations demonstrated the effective reduction in both HOMO-LUMO gap and reaction energy barrier of CO_2* to COOH* by sub-nm Pd skin. We believe that the findings presented in this work is of great significance for the future design of plasmon-enhanced photocatalysts, as well as a better understanding of plasmonic catalysis mechanisms.

CRediT authorship contribution statement

Xibo Zhang: Conceptualization, Methodology, Investigation, Writing - original draft preparat, Writing - review & editing. **Yunyan Fan**: Investigation, Writing - original draft preparation. **Enming You**: Formal analysis. **Zexuan Li**: Investigation. **Yongdi Dong**: Investigation. **Luning Chen**: Investigation. **Ye Yang:** Formal analysis. **Zhaoxiong Xie:** Supervision. **Qin Kuang:** Writing - original draft preparat, Writing - review & editing, Project administration, Funding acquisition. **Lansun Zheng:** Supervision.

Declaration of Competing Interest

The authors declare that they have no known competing financial interests or personal relationships that could have appeared to influence the work reported in this paper.

Acknowledgements

The fundings are the National Key Research and Development Program of China (2017YFA0206801 and 2017YFA0206500), and the National Natural Science Foundation of China (No. 22071202, 21931009, 21721001, 21773190, and 21671163).

Appendix A. Supporting information

Supplementary data associated with this article can be found in the online version at doi:10.1016/j.nanoen.2021.105950.

References

[1] E.E. Benson, C.P. Kubiak, A.J. Sathrum, J.M. Smieja, Electrocatalytic and homogeneous approaches to conversion of CO2to liquid fuels, Chem. Soc. Rev. 38 (2009) 89–99.

[2] J. Bao, G. Yang, Y. Yoneyama, N. Tsubaki, Significant advances in C1 catalysis: highly efficient catalysts and catalytic reactions, ACS Catal. 9 (2019) 3026–3053.

[3] X. Su, X.F. Yang, Y. Huang, B. Liu, T. Zhang, Single-atom catalysis toward efficient CO2 conversion to CO and formate products, Acc. Chem. Res. 52 (2019) 656–664.

[4] L. Liu, S. Wang, H. Huang, Y. Zhang, T. Ma, Surface sites engineering on semiconductors to boost photocatalytic CO_2 reduction, Nano Energy 75 (2020), 104959.

[5] M.D. Porosoff, B. Yan, J.G. Chen, Catalytic reduction of CO2by H2 for synthesis of CO, methanol and hydrocarbons: challenges and opportunities, Energy Environ. Sci. 9 (2016) 62–73.

[6] E.V. Kondratenko, G. Mul, J. Baltrusaitis, G.O. Larrazábal, J. Pérez-Ramírez, Status and perspectives of CO_2 conversion into fuels and chemicals by catalytic, photocatalytic and electrocatalytic processes, Energy Environ. Sci. 6 (2013) 3112–3135.

[7] R.P. Ye, J. Ding, W. Gong, M.D. Argyle, Q. Zhong, Y. Wang, C.K. Russell, Z. Xu, A. G. Russell, Q. Li, M. Fan, Y.G. Yao, CO_2 hydrogenation to high-value products via heterogeneous catalysis, Nat. Commun. 10 (2019) 5698.

[8] X. Dai, Y. Sun, Reduction of carbon dioxide on photoexcited nanoparticles of VIII group metals, Nanoscale 11 (2019) 16723–16732.

[9] P. Christopher, H. Xin, S. Linic, Visible-light-enhanced catalytic oxidation reactions on plasmonic silver nanostructures, Nat. Chem. 3 (2011) 467–472.

[10] C. Kim, S. Hyeon, J. Lee, W.D. Kim, D.C. Lee, J. Kim, H. Lee, Energy-efficient CO_2 hydrogenation with fast response using photoexcitation of CO_2 adsorbed on metal catalysts, Nat. Commun. 9 (2018) 3027.

[11] Y. Li, J. Hao, H. Song, F. Zhang, X. Bai, X. Meng, H. Zhang, S. Wang, Y. Hu, J. Ye, Selective light absorber-assisted single nickel atom catalysts for ambient sunlight-driven CO_2 methanation, Nat. Commun. 10 (2019) 2359.

[12] H. Robatjazi, H. Zhao, D.F. Swearer, N.J. Hogan, L. Zhou, A. Alabastri, M. J. McClain, P. Nordlander, N.J. Halas, Plasmon-induced selective carbon dioxide conversion on earth-abundant aluminum-cuprous oxide antenna-reactor nanoparticles, Nat. Commun. 8 (2017) 27.

[13] M. Ghoussoub, M. Xia, P.N. Duchesne, D. Segal, G. Ozin, Principles of photothermal gas-phase heterogeneous CO2catalysis, Energy Environ. Sci. 12 (2019) 1122–1142.

[14] J. Jia, P.G. O'Brien, L. He, Q. Qiao, T. Fei, L.M. Reyes, T.E. Burrow, Y. Dong, K. Liao, M. Varela, S.J. Pennycook, M. Hmadeh, A.S. Helmy, N.P. Kherani, D. D. Perovic, G.A. Ozin, Visible and near-infrared photothermal catalyzed hydrogenation of gaseous CO2 over nanostructured Pd@Nb2O5, Adv. Sci. 3 (2016), 1600189.

[15] J. Xu, W.-M. Yang, S.-J. Huang, H. Yin, H. Zhang, P. Radjenovic, Z.-L. Yang, Z.-Q. Tian, J.-F. Li, CdS core-Au plasmonic satellites nanostructure enhanced photocatalytic hydrogen evolution reaction, Nano Energy 49 (2018) 363–371.

[16] K. Feng, S. Wang, D. Zhang, L. Wang, Y. Yu, K. Feng, Z. Li, Z. Zhu, C. Li, M. Cai, Z. Wu, N. Kong, B. Yan, J. Zhong, X. Zhang, G.A. Ozin, L. He, Cobalt plasmonic superstructures enable almost 100% broadband photon efficient CO2 photocatalysis, Adv. Mater. 32 (2020), 2000014.

[17] D. Zhang, K. Lv, C. Li, Y. Fang, S. Wang, Z. Chen, Z. Wu, W. Guan, D. Lou, W. Sun, D. Yang, L. He, X. Zhang, All-earth-abundant photothermal silicon platform for CO2 catalysis with nearly 100% sunlight harvesting ability, Sol. RRL 5 (2020), 2000387.

[18] X. Zhang, X. Li, D. Zhang, N.Q. Su, W. Yang, H.O. Everitt, J. Liu, Product selectivity in plasmonic photocatalysis for carbon dioxide hydrogenation, Nat. Commun. 8 (2017) 14542.

[19] L. Zhou, J.M.P. Martirez, J. Finzel, C. Zhang, D.F. Swearer, S. Tian, H. Robatjazi, M. Lou, L. Dong, L. Henderson, P. Christopher, E.A. Carter, P. Nordlander, N. J. Halas, Light-driven methane dry reforming with single atomic site antenna-reactor plasmonic photocatalysts, Nat. Energy 5 (2020) 61–70.

[20] H. Zhang, J. Wei, X.-G. Zhang, Y.-J. Zhang, P.M. Radjenovica, D.-Y. Wu, F. Pan, Z.-Q. Tian, J.-F. Li, Plasmon-induced interfacial hot-electron transfer directly probed by Raman spectroscopy, Chem 6 (2020) 689–702.

[21] U. Aslam, V.G. Rao, S. Chavez, S. Linic, Catalytic conversion of solar to chemical energy on plasmonic metal nanostructures, Nat. Catal. 1 (2018) 656–665.

[22] D.F. Swearer, H. Zhao, L. Zhou, C. Zhang, H. Robatjazi, J.M. Martirez, C. M. Krauter, S. Yazdi, M.J. McClain, E. Ringe, E.A. Carter, P. Nordlander, N.J. Halas, Heterometallic antenna–reactor complexes for photocatalysis, Proc. Natl. Acad. Sci. U. S. A. 113 (2016) 8916–8920.

[23] C.-c Jian, J. Zhang, W. He, X. Ma, Au-Al intermetallic compounds: a series of more efficient LSPR materials for hot carriers-based applications than noble metal Au, Nano Energy 82 (2021), 105763.

[24] C. Zhang, H. Zhao, L. Zhou, A.E. Schlather, L. Dong, M.J. McClain, D.F. Swearer, P. Nordlander, N.J. Halas, Al–Pd nanodisk heterodimers as antenna–reactor photocatalysts, Nano Lett. 16 (2016) 6677–6682.

[25] K. Li, N.J. Hogan, M.J. Kale, N.J. Halas, P. Nordlander, P. Christopher, Balancing near-field enhancement, absorption, and scattering for effective antenna–reactor plasmonic photocatalysis, Nano Lett. 17 (2017) 3710–3717.

[26] V. Flauraud, G.D. Bernasconi, J. Butet, D.T.L. Alexander, O.J.F. Martin, J. Brugger, Mode coupling in plasmonic heterodimers probed with electron energy loss spectroscopy, ACS Nano 11 (2017) 3485–3495.

[27] S. Chavez, V.G. Rao, S. Linic, Unearthing the factors governing site specific rates of electronic excitations in multicomponent plasmonic systems and catalysts, Faraday Discuss. 214 (2019) 441–453.

[28] W. Gao, Q. Liu, X. Zhao, C. Cui, S. Zhang, W. Zhou, X. Wang, S. Wang, H. Liu, Y. Sang, Electromagnetic induction effect induced high-efficiency hot charge generation and transfer in Pd-tipped Au nanorods to boost plasmon-enhanced formic acid dehydrogenation, Nano Energy 80 (2021), 105543.

[29] H. Huang, L. Zhang, Z. Lv, R. Long, C. Zhang, Y. Lin, K. Wei, C. Wang, L. Chen, Z. Y. Li, Q. Zhang, Y. Luo, Y. Xiong, Unraveling surface plasmon decay in core–shell nanostructures toward broadband light-driven catalytic organic synthesis, J. Am. Chem. Soc. 138 (2016) 6822–6828.

[30] U. Aslam, S. Chavez, S. Linic, Controlling energy flow in multimetallic nanostructures for plasmonic catalysis, Nat. Nanotech 12 (2017) 1000–1005.

[31] S. Chavez, U. Aslam, S. Linic, Design principles for directing energy and energetic charge flow in multicomponent plasmonic nanostructures, ACS Energy Lett. 3 (2018) 1590–1596.

[32] P.B. Johnson, R.W. Christy, Optical constants of the noble metals, Phys. Rev. B 6 (1972) 4370–4379.

[33] P. Johnson, R. Christy, Optical constants of transition metals: Ti, V, Cr, Mn, Fe, Co, Ni, and Pd, Phys. Rev. B 9 (1974) 5056–5070.

[34] J.P. Perdew, K. Burke, M. Ernzerhof, Generalized gradient approximation made simple, Phys. Rev. Lett. 77 (1996) 3865–3868.

[35] L. Gong, D. Zhang, C.Y. Lin, Y. Zhu, Y. Shen, J. Zhang, X. Han, L. Zhang, Z. Xia, Catalytic mechanisms and design principles for single-atom catalysts in highly efficient CO2 conversion, Adv. Energy Mater. 9 (2019), 1902625.

[36] Z. Zheng, H. Xu, Z. Xu, A monodispersed spherical Zr-based metal-organic framework catalyst, Pt/Au@Pd@UIO-66, comprising an Au@Pd core-shell encapsulated in a UIO-66 Center and its highly selective CO2 hydrogenation to produce CO, Small 14 (2018), 1702812.

[37] V. Celorrio, P.M. Quaino, E. Santos, J. Flórez-Montaño, J.J.L. Humphrey, O. Guillén-Villafuerte, D. Plana, M.J. Lázaro, E. Pastor, D.J. Fermín, Strain effects on the oxidation of CO and HCOOH on Au–Pd core–shell nanoparticles, ACS Catal. 7 (2017) 1673–1680.

[38] X. Zhang, Y.L. Chen, R.S. Liu, D.P. Tsai, Plasmonic photocatalysis, Rep. Prog. Phys. 76 (2013), 046401.

[39] J.F. Li, Y.J. Zhang, S.Y. Ding, R. Panneerselvam, Z.Q. Tian, Core–shell nanoparticle-enhanced Raman spectroscopy, Chem. Rev. 117 (2017) 5002–5069.

[40] Z. Yin, Y. Wang, C. Song, L. Zheng, N. Ma, X. Liu, S. Li, L. Lin, M. Li, Y. Xu, W. Li, G. Hu, Z. Fang, D. Ma, Hybrid Au–Ag nanostructures for enhanced plasmon-driven catalytic selective hydrogenation through visible light irradiation and surface-enhanced Raman scattering, J. Am. Chem. Soc. 140 (2018) 864–867.

[41] K. Sytwu, M. Vadai, J.A. Dionne, Adv. Phys.: X 4 (2019), 1619480.

[42] B. Rungtaweevoranit, J. Baek, J.R. Araujo, B.S. Archanjo, K.M. Choi, O.M. Yaghi, G.A. Somorjai, Copper nanocrystals encapsulated in Zr-based metal–organic frameworks for highly selective CO2 hydrogenation to methanol, Nano Lett. 16 (2016) 7645–7649.

[43] X. Deng, R. Li, S. Wu, L. Wang, J. Hu, J. Ma, W. Jiang, N. Zhang, X. Zheng, C. Gao, L. Wang, Q. Zhang, J. Zhu, Y. Xiong, Metal–organic framework coating enhances the performance of Cu2O in photoelectrochemical CO2 reduction, J. Am. Chem. Soc. 141 (2019) 10924–10929.

[44] Y. Zhu, J. Zheng, J. Ye, Y. Cui, K. Koh, L. Kovarik, D.M. Camaioni, J.L. Fulton, D. G. Truhlar, M. Neurock, C.J. Cramer, O.Y. Gutierrez, J.A. Lercher, Copper-zirconia interfaces in UiO-66 enable selective catalytic hydrogenation of CO_2 to methanol, Nat. Commun. 11 (2020) 5849.

[45] L. Chen, W. Zhan, H. Fang, Z. Cao, C. Yuan, Z. Xie, Q. Kuang, L. Zheng, Selective catalytic performances of noble metal nanoparticle@MOF composites: the concomitant effect of Aperture size and structural flexibility of MOF matrices, Chem. Eur. J. 23 (2017) 11397–11403.

[46] M. Zhao, K. Yuan, Y. Wang, G. Li, J. Guo, L. Gu, W. Hu, H. Zhao, Z. Tang, Metal–organic frameworks as selectivity regulators for hydrogenation reactions, Nature 539 (2016) 76–80.

[47] D. Chen, W. Yang, L. Jiao, L. Li, S.H. Yu, H.L. Jiang, Boosting catalysis of Pd nanoparticles in MOFs by pore wall engineering: the roles of electron transfer and adsorption energy, Adv. Mater. 32 (2020), 2000041.

[48] Y. Liu, Z. Tang, Multifunctional nanoparticle@MOF core-shell nanostructures, Adv. Mater. 25 (2013) 5819–5825.

[49] G. Lu, S. Li, Z. Guo, O.K. Farha, B.G. Hauser, X. Qi, Y. Wang, X. Wang, S. Han, X. Liu, J.S. DuChene, H. Zhang, Q. Zhang, X. Chen, J. Ma, S.C. Loo, W.D. Wei, Y. Yang, J.T. Hupp, F. Huo, Imparting functionality to a metal–organic framework material by controlled nanoparticle encapsulation, Nat. Chem. 4 (2012) 310–316.

[50] W. Zhang, L. Wang, K. Wang, M.U. Khan, M. Wang, H. Li, J. Zeng, Integration of photothermal effect and heat insulation to efficiently reduce reaction temperature of CO2 hydrogenation, Small 13 (2017), 1602583.

[51] X. Chen, Y. Chen, M. Yan, M. Qiu, Nanosecond photothermal effects in plasmonic nanostructures, ACS Nano 6 (2012) 2550–2557.

[52] J.H. Hodak, I. Martini, G.V. Hartland, Spectroscopy and dynamics of nanometer-sized noble metal particles, J. Phys. Chem. B 102 (1998) 6958–6967.

[53] J. Hodak, I. Martini, G.V. Hartland, Ultrafast study of electron–phonon coupling in colloidal gold particles, Chem. Phys. Lett. 284 (1998) 135–141.

[54] J. Guo, Y. Zhang, L. Shi, Y. Zhu, M.F. Mideksa, K. Hou, W. Zhao, D. Wang, M. Zhao, X. Zhang, J. Lv, J. Zhang, X. Wang, Z. Tang, Boosting hot electrons in hetero-superstructures for plasmon-enhanced catalysis, J. Am. Chem. Soc. 139 (2017) 17964–17972.
[55] J.H. Hodak, A. Henglein, G.V. Hartland, Coherent excitation of acoustic breathing modes in bimetallic core–shell nanoparticles, J. Phys. Chem. B 104 (2000) 5053–5055.
[56] X. Zhang, E. Lim, S.K. Kim, K.H. Bowen, Photoelectron spectroscopic and computational study of (M–CO_2)−anions, M = Cu, Ag, Au, J. Chem. Phys. 143 (2015), 174305.
[57] J. Ko, B.-K. Kim, J.W. Han, Density functional theory study for catalytic activation and dissociation of CO2 on bimetallic alloy surfaces, J. Phys. Chem. C 120 (2016) 3438–3447.
[58] S. Kattel, P. Liu, J.G. Chen, Tuning selectivity of CO2 hydrogenation reactions at the metal/oxide interface, J. Am. Chem. Soc. 139 (2017) 9739–9754.
[59] E.S. Gutterod, A. Lazzarini, T. Fjermestad, G. Kaur, M. Manzoli, S. Bordiga, S. Svelle, K.P. Lillerud, E. Skulason, S. Oien-Odegaard, A. Nova, U. Olsbye, Hydrogenation of CO2 to methanol by Pt nanoparticles encapsulated in UiO-67: deciphering the role of the metal–organic framework, J. Am. Chem. Soc. 142 (2020) 999–1009.

Xibo Zhang received his B.S degree from University of Electronic Science and Technology of China in 2017. Then he continued pursuing his PhD degree at Xiamen University under the supervision of Prof. Qin Kuang. His research focuses on the controlled synthesis of MOF-based materials and their application in catalysis.

Yunyan Fan received his B.S degree from Fuzhou University in China in 2018. Then she continued pursuing his PhD degree at Xiamen University under the supervision of Prof. Ye Yang. Her research focuses on The effect of polaronic effect on photocarrier dynamics in metal oxides.

Enming You received his B.S degree in Physics at Nanjing University in 2015 and a Ph.D. in Chemistry under the supervision of Prof. Zhong-Qun Tian and Prof. Song-Yuan Ding at Xiamen University in 2020. He is currently working as a postdoctoral fellow in Xiamen University. His research interests are surface-enhanced infrared absorption and AFM-based infrared nanospectroscopy and imaging.

Zexuan Li is an undergraduate student at Xiamen University, majored in energy chemistry. He is currently interested in the synthesis of MOF-based materials.

Yongdi Dong received her B.S degree from Xiamen University in 2016. Then she continued pursuing her PhD degree at Xiamen University under the supervision of Prof. Zhaoxiong Xie. Her research focuses on controllable synthesis of noble metal nanocrystals and exploring the structure-activity relationship of copper-based model catalysts in CO_2 electroreduction reaction (CO_2RR)

Luning Chen received his B.S degree from Xiamen University in 2014. Then he continued pursuing his PhD degree at Xiamen University under the supervision of Prof. Lansun Zheng and Prof. Qin Kuang. He is currently working as a visiting scholar in Professor Gabor A. Somorjai's group in Lawrence Berkeley National Laboratory. His research focuses on the controlled synthesis of well-defined MOF-based materials and their application in heterogeneous catalysis.

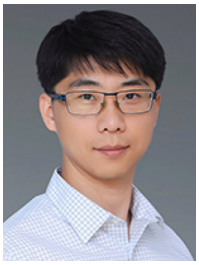

Ye Yang is a professor of chemistry at Xiamen University. He received his B.S. degree from University of Science and Technology of China in 2008 and his PhD degree from Emory University in 2013. His current research interests are in the ultrafast carrier dynamics in, molecular complex, semiconductors and transition metal oxides.

Zhaoxiong Xie received his B.S., M. S. and PhD degrees from department of chemistry, Xiamen University in 1987, 1990 and 1995, respectively. Since 2002, he holds the position of Professor of physical chemistry at Xiamen University. He won the National Distinguished Young Scientist Fund of China in 2007 and Chang Jiang Chair Professorship in 2014. His current research interests are focused on surface/interfacial chemistry of functional inorganic nanomaterials.

Qin Kuang is a professor of Chemistry at Xiamen University. He received his B.S (2001) and PhD (2008) in Chemistry from Xiamen University. He worked as a postdoctoral research fellow at Hong Kong University of Science and Technology from 2011 to 2012. His research focuses on the surface/interface engineering of inorganic functional nanomaterials and their applications in energy and environmental fields.

Lansun Zheng is a professor of Chemistry at Xiamen University. He received his B.S degree from Xiamen University in 1982 and his PhD degree from Rice University, USA in 1986. He was selected as academicians of Chinese Academy of Sciences in 2001. His research interests include cluster science, mass spectrometry, and nanomaterials.